1 **Mesoporous Si and multi-layered Si/C films by Pulsed Laser Deposition as Li-ion**

2 **microbattery anodes**

3 Nadia Garino[a], Erika Biserni[b,c], Andrea Li Bassi[b,c], Paola Bruno[c], Claudio Gerbaldi[*,d]

4 *[a] Center for Space Human Robotics @Polito, Istituto Italiano di Tecnologia, Corso*

5 *Trento 21, 10129 Torino, Italy*

6 *[b] Department of Energy, Politecnico di Milano, Via Ponzio 34, 20133 Milano, Italy*

7 *[c] Center for Nano Science and Technology @PoliMi, Istituto Italiano di Tecnologia, Via*

8 *Pascoli 70/3, 20133 Milano, Italy*

9 *[d] GAME Lab, Department of Applied Science and Technology – DISAT, Institute of*

10 *Chemistry, Politecnico di Torino, Corso Duca degli Abruzzi 24, 10129 Torino, Italy*

11 * Corresponding author (C. Gerbaldi). Tel.: +39 011 090 4643; fax: +39 011 090 4699.

12 e-mail address: claudio.gerbaldi@polito.it

13 **Abstract.** Silicon is a very attractive Li-ion battery anode material due to its high

14 theoretical capacity, but proper nanostructuring is needed to accommodate the

15 large volume expansion/shrinkage upon reversible cycling. Hereby, novel

16 mesoporous Si nanostructures are grown at room temperature by simple and rapid

17 Pulsed Laser Deposition (PLD) directly on top of the Cu current collector surface.

18 The samples are characterised from the structural/morphological viewpoint and

19 their promising electrochemical behaviour demonstrated in lab-scale lithium cells.

20 Depending on the porosity, easily tuneable by PLD, specific capacities

21   approaching 250 µAh cm^{-2} are obtained. Successively, newly elaborated bi-

22   component silicon/carbon nanostructures are fabricated in one step by alternating

23   PLD deposition of Si and C, thus resulting in novel multi-layered composite

24   mesoporous films exhibiting profoundly improved performance. Alternated

25   deposition of Si/C layers by PLD is proven to be a straightforward method to

26   produce multi-layered anodes in one processing step. The addition of carbon and

27   mild annealing at 400 °C stabilize the electrochemical performance of the Si-

28   based nanostructures in lab-scale lithium cells, allowing to reach very stable

29   prolonged reversible cycling at improved specific capacity values. This opens the

30   way to further reducing processing steps and processing time, which are key

31   aspects when upscaling is sought.

33   **Introduction**

34 In the last decade, we are dealing with the rapid development of high performing

35 portable electronic devices, such as smart phones and notebooks, which are becoming

36 more and more demanding in terms of energy requirements. This continuously leads to a

37 strong demand for new sources of power able to provide high capacity and high energy

38 densities. In such a scenario, the Li-ion battery (LIB) is recognized as the system of

39 choice. Today's LIBs partially satisfy the present demands, but there is still room for

40 further improvements[1].

41 As far as the anode material is concerned, commercial graphite shows excellent capacity

42 retention during battery cycling. Nevertheless, despite its good cycling stability and low

43 cost, the low theoretical capacity of 372 mAh g^{-1} is clearly insufficient for the huge

44 demands of the next generation of high energy density electronic devices as well as

45 electric vehicles[2]. To meet these requirements, several elements that can reversibly alloy

46 with lithium were investigated, including Si, Sn, Al, Ge, as well as mixed compounds

47 thereof[3–6]. Because of its exceptional theoretical capacity exceeding 4000 mAh g^{-1},

48 silicon is one of the most promising candidates among these elements to be used as

49 anode material, as demonstrated by the intensive investigations recently carried out on

50 this subject. The main limitations to its wide spread application are the extremely high

51 volume change (~300 %)[7] occurring during reversible reaction with lithium and leading

52 to mechanical fragmentation and active material particle pulverization. Nanostructuring,

53 introduction of voids and addition of other active materials having lower capacity (e.g.,

54 carbon) are the main routes currently under exploitation to bypass this drawback. The

55 advantages of nanostructuring have been evidenced in recent works, which demonstrated

56 the existence of a threshold dimension in silicon particles that prevents from crack

57 propagation upon lithiation[8–10]. The introduction of pores in the silicon anodes is another

58 well-known strategy to face the detrimental effects of volume variation[11–13]; indeed,

59 depending on their size and distribution, voids can accommodate the expansion during

60 lithiation, mitigate internal stresses and possibly prevent from fragmentation and

61 detachment from the current collector. Porous Si films are generally prepared via

62 electrochemical etching using hydrofluoric acid [14,15] or by electrodeposition[16–18].

63 In this work, we explore the possibility of growing mesoporous hierarchical amorphous

64 silicon nanostructures by simple and rapid Pulsed Laser Deposition (PLD). As it allows

65 to easily tailor the film morphology at the nanoscale, both in terms of nanostructuration

66 and introduction of voids, PLD enables a straightforward engineering of the anode

67 material properties. In our silicon anodes, we introduced a controlled porosity to buffer

68 the volume expansion; moreover, the preferential growth in the direction perpendicular to

69 the substrate headed to favouring the electronic and ionic transport through the electrode.

70 Different films were fabricated having different morphology and degree of porosity. The

71 effect of an increasing porosity was studied at ambient temperature by electrochemical

72 testing in lithium cell configuration with liquid electrolyte. The best performing sample

73 allowed for good initial capacity over the initial 30 galvanostatic discharge/charge cycles.

74 Successively, in order to improve the electrochemical behaviour, both in terms of overall

75 specific capacity output as well as capacity retention and stability upon prolonged cycling,

76 novel multi-layered Si-C nanostructured composite films were produced. Graphite-like C

77 has the role to improve the overall electrical conductivity (intermediate layers) and to

78 promote the formation of a stable SEI (top layer). Moreover, mild annealing at 400 °C

79 was adopted on these structures, in order to improve the mechanical properties in terms of

80 stress relaxation and adhesion to the Cu current collector, thus to effective increase the

81 stability upon cycling.

82 A previous work by some of the authors demonstrated good electrochemical

83 performances of an anode made by a mesoporous Si film grown by PLD covered by a C

84 layer grown by Chemical Vapour Deposition at 800°C[19]. Here we deeper investigate the

85 properties of mesoporous Si grown by PLD, on the way to optimize the film for

86 microbattery anodes. Based on this optimization, we propose a simplified process to

87 obtain novel multilayered Si/C film where Si and C are both deposited by PLD, followed

88 by a mild annealing at 400°C. Reducing processing steps and processing time is one of

89 the key aspects when upscaling is sought.

90 **Methods**

91 <u>Preparation of mesoporous Si films</u>

92 Mesoporous Silicon films were grown by PLD under ambient conditions. A rotating and

93 translating Si crystalline wafer (monocrystalline CZ, n^+-doped <100>) was ablated by a

94 KrF pulsed laser (248 nm, ~5 J cm^{-2}, 20 Hz, target-to-substrate distance 50 mm) under

95 controlled atmosphere (mixture of < 3 % vol. H_2 in Ar as background gas) in a vacuum

96 chamber, previously evacuated at 3×10^{-3} Pa. In order to grow films having different

97 morphology and porosity, samples were produced under varying background pressures of

98 40, 60 and 100 Pa, respectively. Correspondingly, samples are named Si-40, Si-60 and

99 Si-100, where the number is the deposition pressure for Si. Deposition times were set to

100 obtain film thickness of 1μm. By increasing the background gas pressure, higher porosity

101 can be introduced in the film by means of inducing the formation of bigger clusters

102 during flight with a lower kinetic energy and, hence, a less-packed film on the substrate.

103 Details on the relationship between process parameters and morphology of the Si films

104 are reported in a previous work[20].

105 After native oxide removal by means of citric acid, copper discs were used as a substrate

106 for Si deposition, so to act as the current collector for the active anode material in lithium

107 cell.

108   Fabrication of multi-layered composite Si-C films

109   Composites films with desired morphology were grown by PLD adjusting the

110   background gas pressure (Ar:H_2) for each deposition, so that cluster nucleation and

111   growth could be to some extent controlled and, hence, the film porosity. Si was deposited

112   under 40Pa Ar:H_2, while C was deposited at 5Pa Ar:H_2 (namely, sample Si/C-40).

113   Deposition time for C was fixed to obtain a 70 nm-thick layer, i.e. one third of the ~200

114   nm-thickness of each coupled Si-C layer, while for Si layers grown at different pressures

115   the deposition time was tuned to have a ~130 nm-thick layer, thus obtaining a final

116   overall film thickness of 1 μm. This 1 μm thickness was chosen to allow for comparison

117   with the other approaches described in this article, while the parameters for deposition of

118   C (i.e., gas pressure and time) were set so as to obtain a uniform layer able to cover the

119   underlying Si. The C-layer relative thickness was a non-optimized starting point

120   balancing on the one hand the need for a well-defined C layer, possibly able to pin Si

121   expansion, and on the other hand to have enough Si to consider the final anode as Si-

122   based. We chose to deposit Si and C by means of two separate targets mounted on a

123   switchable target holder to grow alternatively Si or C into a multi-layered composite film.

124   After deposition of the desired amount of one material, the laser was stopped for a while

125   and the target holder switched without opening the vacuum chamber, thus exposing the

126   other target to ablation. The resulting multi-layered sample was then annealed in a closed

127   furnace filled with Ar:H_2 to relieve internal mechanical stresses and possibly promote

128   adhesion of the Si layer to the copper substrate, as proven by experimental results

129   described in ref. [19]. The heating rate was set at 4 °C min^{-1} up to the temperature of

130   400 °C, hold for 5 minutes at 400 °C and then let cool down.

131 <u>Characterization of the materials</u>

132 In order to characterize their morphology and thickness, cross-sectional views of the

133 single- as well as multi-layered Si films were acquired by a Supra 40 Zeiss Field

134 Emission Scanning Electron Microscope (FESEM, accelerating voltage 3-5 kV).

135 Specific surface area (SSA) was determined on a Quadrasorb evo™ (Quantachrome

136 Instruments) using the Brunauer, Emmet, Teller (BET) method. Prior to adsorption,

137 approximately 100.0 mg of solid were placed in the cell and evacuated at about 50 °C for

138 2 h and, successively, at 200 °C for 3h.

139 Raman spectra were acquired on the Si and Si/C samples upon excitation by the second

140 harmonic (532 nm) of an air-cooled Nd:YAG laser. Laser power was kept below 0.4 mW

141 (sample surface) while sampling Si films, in order to avoid laser-induced annealing

142 effects. Spectra were recorded in the range 100-1800 cm^{-1} in the Stokes region and were

143 calibrated against the 520.5 cm^{-1} line of an internal silicon wafer reference. The signal-

144 to-noise ratio was enhanced by repeated acquisitions.

145 Van der Pauw measurements were performed on the samples Si/C-40 either annealed or

146 not, in order to estimate the film conductivity in the two cases. The measurement was

147 carried out at ambient conditions by a Hall Effect measurement Instrument (Microworld-

148 HMS5300, heated stage AMP55), equipped with a permanent magnet (0,5T) and golden

149 fingers with applied current below 20nA.

150 The electrochemical response in liquid electrolyte of the samples was tested in

151 polypropylene three-electrode T-cells assembled as follows: a Si film disk (area 0.785

152 cm^2) as the working electrode, a 1.0 M lithium hexafluorophosphate (LiPF$_6$, Solvionic,

153 France, battery grade) in a 1:1 w/w mixture of ethylene carbonate (EC) and dimethyl

154 carbonate (DMC) electrolyte solution soaked on a Whatman® GF/A separator and a

155 lithium metal foil (high purity lithium foils, Chemetall Foote Corporation) as the counter

156 electrode. For cyclic voltammetry (CV), a second lithium foil was added at the third hole

157 of the cell, in direct contact with the electrolyte, acting as the reference electrode.

158 Galvanostatic discharge/charge cycling (cut off potentials: $0.02 - 1.5$ V vs. Li^+/Li) and

159 CVs (between 0.02 and 1.5 V vs. Li^+/Li, at 0.1 mV s^{-1}) were carried out at ambient

160 temperature on an Arbin Instrument Testing System model BT-2000. Clean electrodes

161 and fresh samples were used for each test. Procedures of cell assembly were performed

162 in the inert atmosphere of a dry glove box (MBraun Labstar, O_2 and H_2O content < 1

163 ppm) filled with extra pure Ar 6.0.

164 **Results and discussion**

165 <u>Characterization of mesoporous Si films</u>

166 In the present work, a very simple single-step PLD process allowed to obtain vertically

167 oriented thin films of mesoporous nanostructured silicon, as evidenced by FESEM

168 analysis for morphological characterisation. The length of the columnar nanostructures

169 was found to be approximately 1 μm, as shown in images (a), (c) and (e) of Figure 1,

170 where the low magnification cross-sectional views of the different amorphous silicon

171 films are depicted.

172
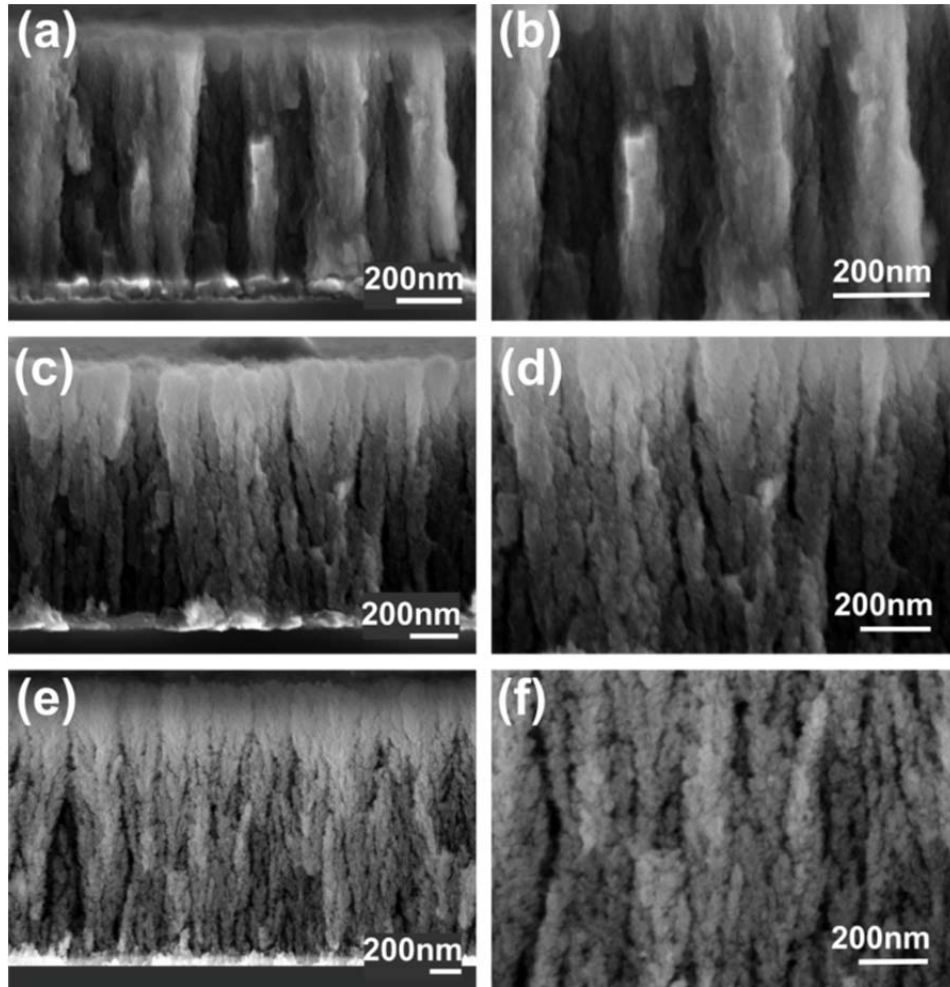
Figure 1 Cross-sectional FESEM images showing the different morphology of the mesoporous single-layered Si nanostructured films grown at increasing background gas pressure: (a, b) 40Pa, (c, d) 60Pa, (e, f) 100Pa.

The fabrication method was chosen and tuned to grow hierarchical films featured by aggregation of clusters in a columnar mesoporous algae-like structure (see images b, d, f in Figure 1). This was meant, on the one hand, to introduce some degree of porosity, thus accounting for volume expansion of lithiated silicon and, on the other hand, to address the need for overall mechanical integrity. In addition, the anisotropic, columnar structure could in principle promote faster kinetics and more effective electronic transport

182 throughout the whole electrode thickness as well as hinder the segregation of particles

183 during electrochemical operation.

184 An estimate of the densities of these films is provided in a previous work,[20] with a value

185 of 0.36 g cm^{-3} for the sample 100 Pa, 0.92 g cm^{-3} for 60 Pa and 1.66 g cm^{-3} for 40 Pa. If

186 compared to the density of bulk silicon (i.e., 2.33 g cm^{-3}), these result in estimated

187 porosities of about 85, 60 and 29 %, respectively.

188 Accurate determination of specific surface area (SSA) in porous Si is usually performed

189 through BET technique, which analyses the adsorption/desorption isotherms of gases at

190 low temperature.[21] Nitrogen adsorption-desorption isotherms, shown in Figure 2 (a-c),

191 are mainly classified as type IV isotherms with a hysteresis loop.[22] This type of isotherm

192 denotes a mesoporous material (pore diameters of 2–50 nm) with the hysteresis loop

193 being associated with the capillary condensation of nitrogen within the mesopores. In

194 details, the relative pressure at which the hysteresis of adsorption/desorption is recorded

195 in the isothermal profiles may account for the different pore size distribution in films

196 having different morphology. By comparing BET data of Figure 2 with FESEM images

197 shown in Fig. 1, two orders of porosity can be traced in each of the three films. The

198 "first-order" porosity is the one given by large intra-algae pores with diameter size in the

199 range of tens of nanometers and gives rise to the hysteresis in the low partial pressure

200 range of the isotherms. The "second order" porosity is instead the one of voids between

201 clusters composing each single algae of the film; these have a diameter in the range up to

202 tens of nanometers and are represented by the hysteresis in the high partial pressure range

203 of the isothermal profile. In sample 40Pa, the "first order" porosity dominates the overall

204 porosity, as from the position of the hysteresis in the isothermal profile as well as

205 visually confirmed by FESEM analysis.
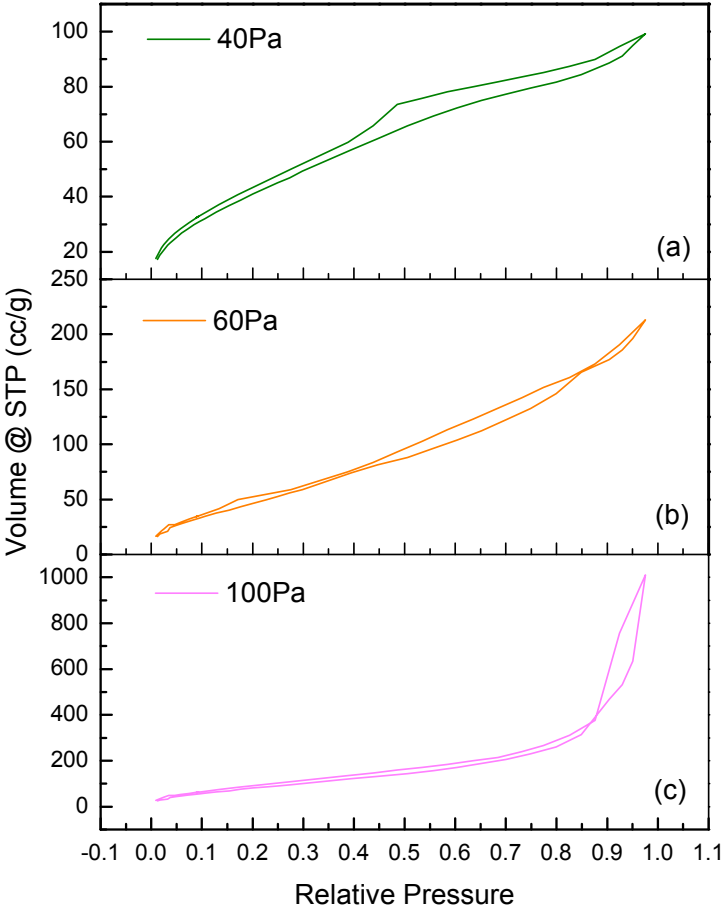
206

207 **Figure 2** Isothermal profiles of single-layered Si films prepared at increasingly higher

208 applied deposition pressures: (a) 40Pa, (b) 60Pa, (c) 100Pa.

209 On the contrary, the "second" order porosity becomes more important in films produced

210 at higher pressure. As a consequence, the hysteresis in the isotherms shifts towards the

211 range of higher partial pressures; this is particularly evident in sample Si-100, where

212 almost only the "second" order porosity is present. Exploiting the BET theory, the

213 following values of specific surface area were obtained for each sample prepared varying

214 the deposition pressure: 68, 109 and 189 $m^2\ g^{-1}$ for sample Si-40, Si-60 and Si-100,

215 respectively. As expected, surface area values increase almost linearly with the increase

216 in the applied deposition pressure from 40 to 100 Pa, in good agreement with SEM

217 analysis and with previous literature on porous films of silicon or other materials

218 prepared by PLD.[23,24]

219 Raman analysis on the as-prepared single-layered Si nanostructured anodes before

220 electrochemical tests reveals the amorphous character of their structure (see Fig. 3, where

221 only the Raman spectrum of sample 40Pa is shown as representative for the three

222 samples prepared), as from the characteristic Gaussian bands centred around 145, 330,

223 430 and 490 cm^{-1} that are generally attributed to the transverse acoustic (TA),

224 longitudinal acoustic (LA), longitudinal optic (LO) and transverse optic (TO) modes of

225 amorphous Si, respectively.[25]
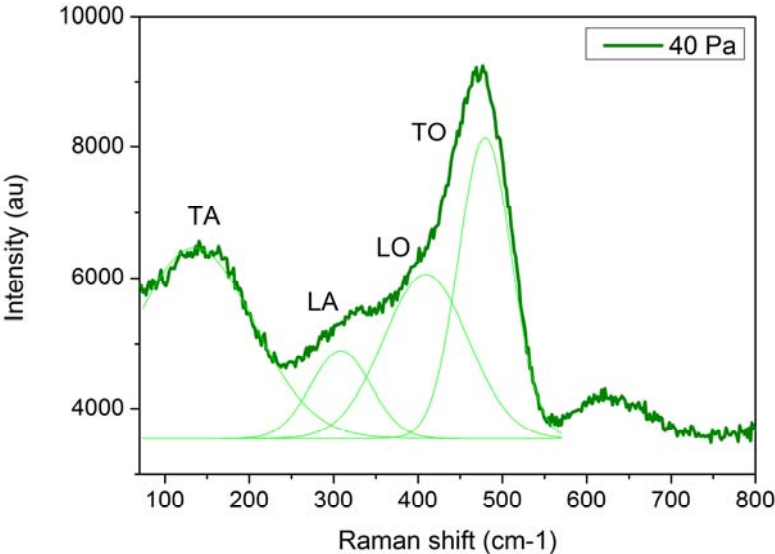
226

227 **Figure 3** Raman spectrum of Si-40 (thick line), fitted by the characteristic Gaussian
228 curves of amorphous silicon (thin lines).

229　In samples produced at 100 Pa, an additional peak at 515 cm^{-1} was detected, being

230　attributed to the transverse optic (TO) mode of silicon crystals of nanometric size, in

231　agreement with the literature[26–28] and with the capability, demonstrated in previous works,

232　to grow Si nanocrystals by PLD (2.5 to 6 nm), embedded in an amorphous matrix[20].

233　The ambient temperature electrochemical behaviour was evaluated in laboratory-scale

234　lithium test cells and carried out by means of cyclic voltammetry and galvanostatic

235　discharge/charge cycling at various current regimes. Results are shown in the plots of

236　Figure 4 (a-c). Note that the electrodes were used as-grown on the Cu current collector,

237　without any addition of binders and/or conducting additives.

238　The typical cyclic voltammetric response of the porous silicon nanostructures prepared

239　by PLD is shown in Figure 4 (a) in its initial 10 cycles. Sample deposited at 40 Pa is

240　representative for the complete set of samples here prepared. It was performed at the scan

241　rate of 0.1 mV s^{-1} between 0.02 and 1.5 V vs. Li^{+}/Li. The cyclic voltammograms (CV)

242　show the typical behaviour of silicon electrodes upon reversible alloying/dealloying

243　reactions with lithium ions,[29,30] resulting in two main couples of anodic and cathodic

244　peaks. In details, in the initial scan towards lower potential values, it shows two cathodic

245　peaks at below 0.2 V vs. Li^{+}/Li (i.e., around 0.15 V as the dominant, and around 0.05 V),

246　characteristics of the lithiation step into amorphous silicon. These are reflected in the

247　following anodic scan, where the two corresponding broad anodic peaks, centred at about

248　0.3 V and 0.47 V vs. Li^{+}/Li, indicate a two-step lithium extraction process from the Li–Si

249　alloy back to amorphous Si. In the second cathodic scan, the broad cathodic peaks

250　slightly shift towards higher potential values (e.g., the dominant centred at ca. 0.18 V). It

251　is supposed to come from a slightly different kinetics in the alloying process due to the

252   formation of slightly different metastable amorphous Li_xSi phases according to the

253   previous literature[31].

254
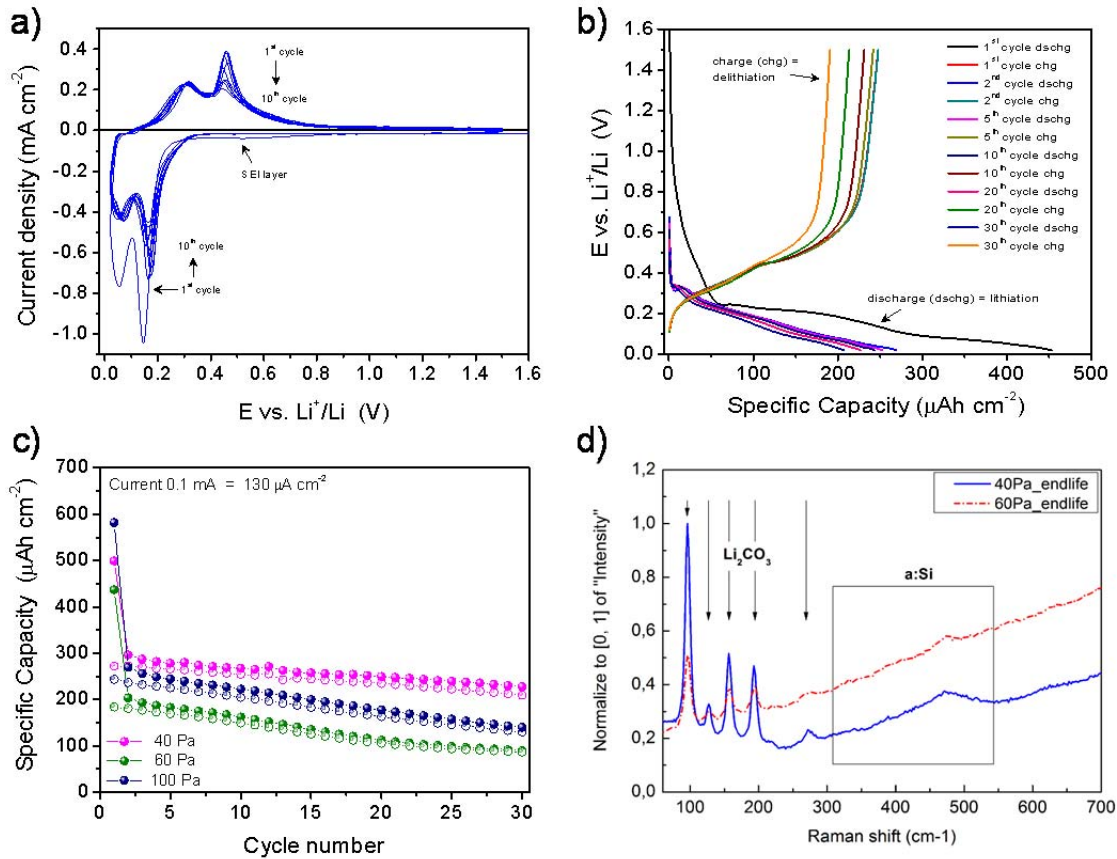
Figure 4 Ambient temperature electrochemical behaviour in lab-scale lithium test cells
of as-grown mesoporous single-layered Si nanostructures: (a) cyclic voltammetry (cycles
1-10) of sample 40Pa in the potential range of 0.02–1.5 V vs. Li^+/Li at a scan rate of 0.1
mV s^{-1}, (b) galvanostatic discharge/charge potential vs. specific capacity profiles of
sample 40Pa at 130 µA cm^{-2}, (c) specific capacity vs. cycle number of the three samples.
Moreover, in (d) the Raman spectra taken on Si-40 and Si-60 anodes after
electrochemical tests are shown (together with the large band of amorphous silicon, the
peaks of Li_2CO_3 are highlighted).

263   Regarding the formation of the solid electrolyte interphase (SEI) layer, it appears in the

264   first cathodic scan as a broad faint signal between 0.6 and 0.4 V vs. 🗨/Li.

265 The potential vs. ~~time~~ profiles upon discharge (lithiation) and charge (delithiation) for

266 sample 40 Pa, are shown in plot (b) of Figure 4. The charge/discharge current rate used

267 for each sample was 0.1 mA, corresponding to about 130 μA cm^{-2}. Profiles show the

268 typical features of amorphous silicon electrodes, with an initial discharge cycle being

269 rather different from the following ones due to the formation of the SEI layer and to the

270 presence of high oxygen content at the surface of the electrode, as usual for amorphous

271 silicon nanoparticles. This causes the relatively large irreversible capacity loss, which

272 always results in low initial Coulombic efficiency for these kind of electrode materials.

273 The cycling performance of the mesoporous single-layered Si nanostructures in lab-scale

274 lithium test cells is shown in Figure 4(c). The initial 30 galvanostatic cycles account for

275 good initial capacity higher than 200 μAh cm^{-2} for all of the three porous films, with a

276 capacity loss of about 40 % for sample 40 Pa and 50 % for both 60 Pa and 100 Pa upon

277 initial lithiation; this is a reasonably low value for initial capacity decay if compared to

278 similar high-surface-area silicon nanostructures reported in the literature[30]. Based on the

279 kind of synthesis adopted in the present work, the sample having lower surface area

280 available for reaction with the electrolyte, i.e. the one prepared at a pressure of 40 Pa,

281 shows in fact lower capacity loss during initial lithiation. This is reflected also in the

282 overall electrochemical behaviour, which is superior both in terms of higher specific

283 capacity values and stability upon reversible cycling, and results in the highest value of

284 capacity retention (around 77 %) after 30 discharge/charge cycles in lithium cell.

285 After electrochemical tests, some of the cells were opened to characterize their status

286 after-cycling. Representative Raman spectra of the anodes were acquired after their

287 washing in EC:DEC in order to remove residuals from the electrolyte as well as glass-

288 fibres from the separator. In addition to the bands of amorphous silicon, the spectra

289 reveal on all of the samples the presence of intense and sharp peaks at 96, 127, 156, 193,

290 273 cm^{-1} that constitute the fingerprint of lithium carbonate (Li_2CO_3). As reported in

291 several studies in the literature, Li_2CO_3 comes from the electrolyte decomposition in

292 those systems that use $LiPF_6$ as the salt dissolved [24–27].

293 <u>Multi-layered Si/C bi-component films</u>

294 In order to improve the cycling performance of the newly elaborated silicon

295 nanostructures, the sample having the most promising prospects in terms of galvanostatic

296 cycling, namely Si-40, was successively prepared in the form of a multi-layered

297 nanocomposite film where Si-40 layers were alternated to C ones. In this way, multi-

298 layered structures were grown where Si and C were alternated 9 times (10 layers, 5

299 couples Si-C), starting with Si in contact with the copper collector and terminating with

300 C on top of the whole stack. The role of the C top layer is to promote the formation of a

301 stable SEI being in direct contact with the electrolyte, while the C layers in between of

302 the stack are meant to improve the overall electrical conductivity and buffer the volume

303 expansion of the Si layers. The multi-layered sample was then annealed at 400 °C for 5

304 minutes in inert atmosphere. The annealing treatment is thought to be effective for

305 internal stress relaxation and is supposed to improve the adhesion of the Si film onto the

306 copper substrate.

307
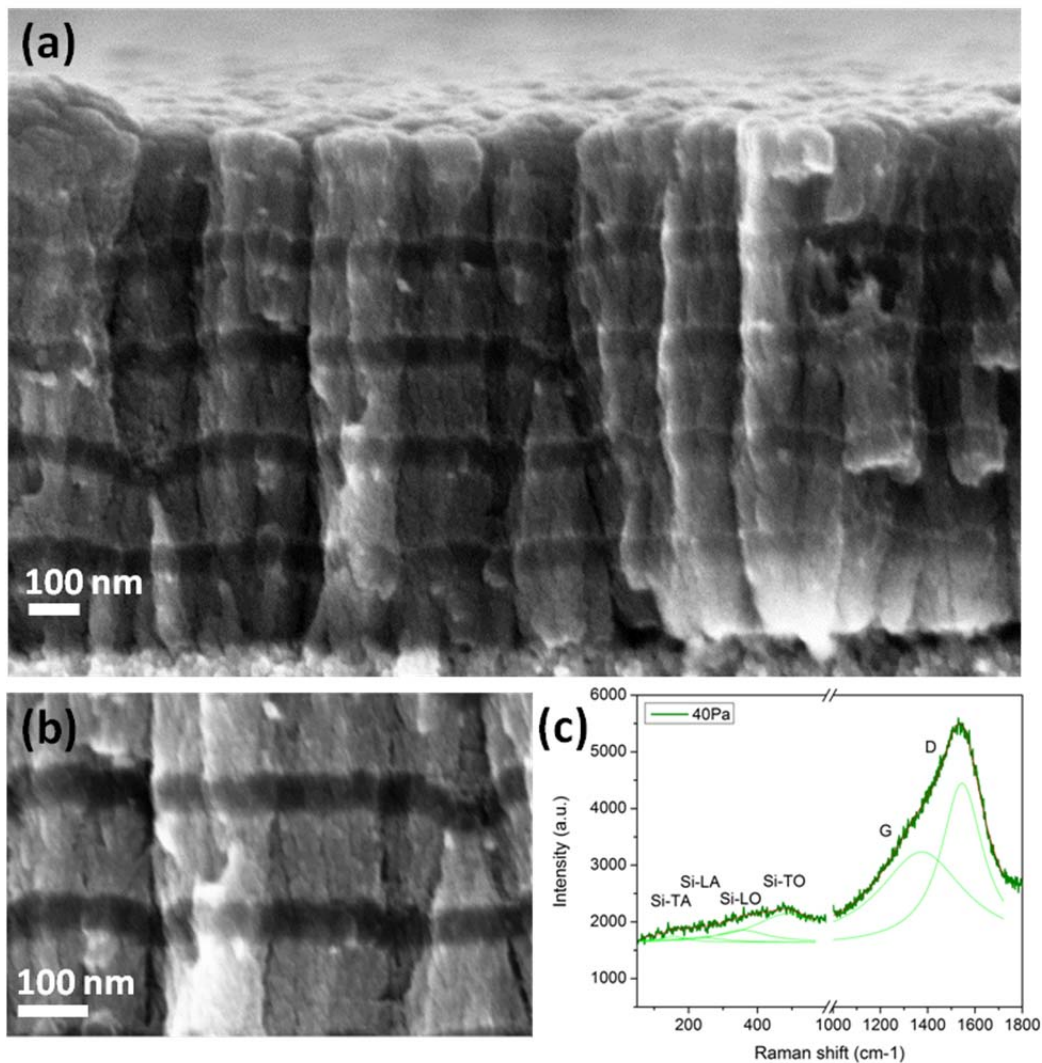
Figure 5 (a,b) Cross-sectional views at different magnification and (c) Raman spectrum of the multi-layered Si/C-40 film.

Cross-sectional views of the multi-layered Si/C-40Pa film acquired at different magnifications are shown in Figure 5(a,b). The alternated Si and C stacks are clearly visible for this sample, where silicon was grown at 40Pa, unlike the more porous samples with Si deposited at higher pressures (not shown here). Probably, the higher porosity of the single Si layer provides a rough surface for the deposition of C, which can then infiltrate into Si instead of forming a separate layer.

316   Raman investigation on multilayered samples is discussed upon considering the spectral

317   range as divided into two parts: the one containing the features arising from Si layers

318   (100-600 cm^{-1}), the other one accounting for C layers (1000-1800 cm^{-1}). In the range

319   100-600 cm^{-1} (left-hand side of the spectrum in Figure 5c), Raman spectra recorded on

320   as-deposited samples show the characteristic features of amorphous Si, i.e. the bands

321   related to the transverse acoustic (TA), longitudinal acoustic (LA), longitudinal optic

322   (LO) and transverse optic (TO) modes[25], respectively, as in the case of single-layered

323   samples. For multilayered samples, the spectral region between 1000 and 1800 cm^{-1} was

324   also considered, and the spectra were fitted with four Gaussian curves, following the

325   procedure described by Ferrari et al.[36]. The right-hand side of the spectrum in Figure 5(c)

326   features the two typical bands of amorphous graphitic carbon, the one intense and broad

327   around 1330 cm^{-1} (D band) and the narrower one around 1540 cm^{-1} (G band), this latter

328   being associated to the in-plane stretching of sp^2 bonds. D band, instead, arises from the

329   breathing mode of C-rings in disordered layers, e.g. from distorted 6-folded rings or from

330   rings of different order[36,37].

331   Van der Pauw measurements were performed on the multi-layered Si/C-40Pa sample

332   either annealed or not, in order to estimate the film conductivity in the two cases. As

333   summarized in Table 1, the annealed samples show a 10-times smaller resistivity with

334   respect to the non-annealed ones. It is not straightforward to extract a value of

335   conductivity from these measurements, due to the inhomogeneous structure of the film

336   (i.e., a nanostructured nanoporous assembly) and, hence, the resistivity and conductivity

337   should be considered as effective quantities, viz. obtained by considering the film as

338   composed by an effective uniform 1μm-thick medium.

Sample	Eff. Resistivity (Ω cm)	Eff. Conductivity $(\Omega$ cm$)^{-1}$
Si/C-40 annealed	1.37E+03	7.29E-04
Si/C-40 not annealed	1.33E+04	7.51E-05

339 **Table 1.** Van der Pauw measurements on multi-layered Si/C-40, annealed and not-

340 annealed.

341 The annealed multi-layered Si/C-40 nanocomposite film was then tested under the same

342 constant current conditions as for the single-layered samples (i.e., 0.1 mA, viz. about 130

343 μA cm^{-2}) between 0.02 V and 1.5 V (vs. Li$^+$/Li). The cycling response at ambient

344 temperature is shown in Figure 6, where both the charge/discharge potential vs. specific

345 capacity profiles (graph a) and specific capacity vs. cycle number along with Coulombic

346 efficiency (graph b) are plotted. In general, annealed samples showed good cyclability.

347 The initial capacity of about 400 μAh cm^{-2} is lost at only 15 % during the first cycle and

348 then rapidly stabilizes slightly above 300 μAh cm^{-2} in the following cycles. Noteworthy,

349 the specific capacity exceeds 295 μAh cm^{-2} after prolonged operation of 100

350 discharge/charge cycles. Clearly, if compared to the corresponding single-layered Si

351 sample shown in Fig. 4, both a noticeable increase in the overall specific capacity as well

352 as a profound improvement in the stability upon prolonged cycling was successfully

353 obtained. Also the Coulombic efficiency rapidly reaches 99 % after the initial cycles and

354 then stabilizes. It is noteworthy that galvanostatic charge/discharge curves of the

355 reference samples (not annealed) were affected by a sudden drop in capacity during the

356 initial cycles, with rapid cell failure. Thus, as expected, the annealing step proved to be

357   beneficial for the stability of the anodes, confirming the explanations provided in the

358   literature about CVD-induced effects[38]. Moreover, the role of the top layer of carbon in

359   promoting the formation of a stable SEI is confirmed by the much more limited specific

360   capacity loss upon initial lithiation (below 15 %), if compared to the much more

361   pronounced irreversible capacity loss exceeding 40 % demonstrated by the corresponding

362   mesoporous single-component Si film.
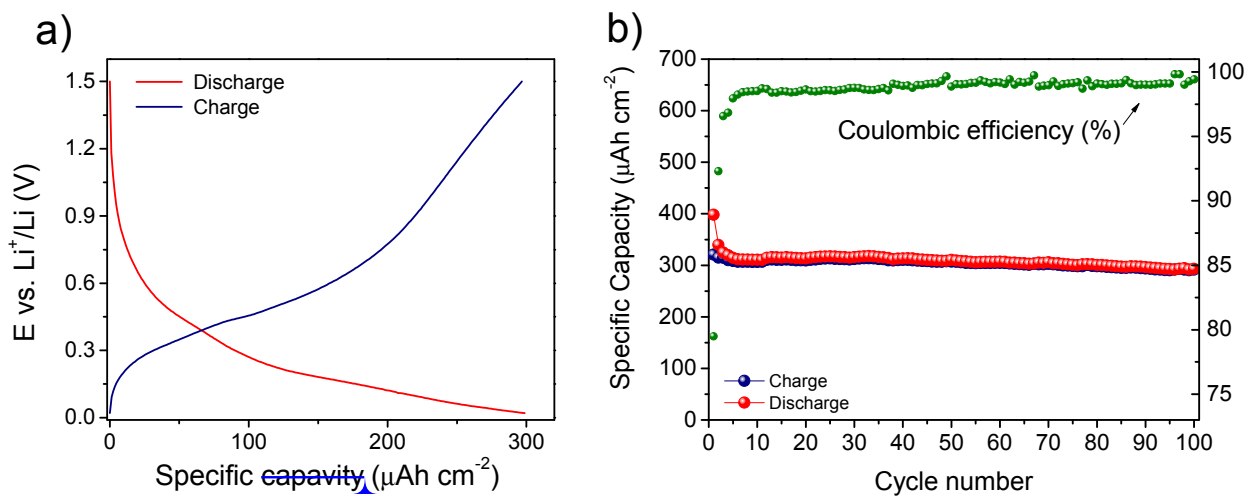
363

364   **Figure 6** Ambient temperature galvanostatic cycling behaviour of the annealed multi-
365   layered Si/C-40 nanocomposite film at 130 $\mu A\ cm^{-2}$: (a) representative constant current
366   discharge/charge potential vs. specific capacity profiles (100th cycle), (b) specific
367   capacity vs. cycle number along with Coulombic efficiency.

368   The results obtained clearly indicate that the multi-layered bi-component Si/C films

369   prepared by sequential PLD deposition at 40Pa and successively annealed at 400 °C own

370   a great potential to be used as a high capacity, highly stable anode material in the next-

371   generation of lithium-based (micro)batteries.

372   **Conclusions**

373   Silicon is very attractive as active material for Li-ion battery anodes due to its high

374   theoretical capacity, but proper nanostructuration is needed to accommodate the large

375   volume expansion/shrinkage upon reversible cycling. This would overcome the

376   disgregation induced by the lithiation/delithiation processes, often resulting in poor long-

377   term performance.

378   In this work, mesoporous nanostructured silicon anodes were fabricated by Pulsed Laser

379   Deposition technique, characterised and electrochemically tested in lab-scale lithium test

380   cells. Different deposition pressures were exploited in order to evaluate the influence of

381   this process parameter on the morphological/electrochemical characteristics of the

382   resulting nanostructures. The sample prepared at lower deposition pressure, having

383   porosity featured by larger average pore size and lower surface area, showed initial

384   capacity approaching 250 µAh cm^{-2} upon 30 galvanostatic discharge/charge cycles. We

385   believe that the higher stability of the samples deposited at lower pressure can be related

386   to their lower surface area. On the contrary, the higher surface area of the more porous

387   samples (samples 60 Pa and 100 Pa) is likely to be responsible for their increased

388   capacity fade; more surface area is involved, in fact, in the side reactions with the

389   electrolyte and, hence, more capacity is lost in forming the interphase layer. The

390   appearance of intense peaks attributed to Li_2CO_3 in the Raman spectra confirms that

391   losses due to the SEI formation are relevant to the proper operation of the single-layered

392   films.

393   Moreover, alternated deposition of Si/C layers by PLD has proven to be a straightforward

394   method to produce multi-layered bi-component electrode films in one processing step.

395 The addition of carbon and mild annealing at 400 °C stabilized the electrochemical

396 performance in lithium cells: compared to the corresponding single-layered Si sample,

397 both a noticeable increase in the overall specific capacity as well as a very profoundly

398 improved stability upon prolonged cycling has been successfully obtained. The beneficial

399 impact of an increased conductivity upon annealing may have a role in the improved

400 electrochemical performances of the annealed silicon anodes, as it can promote faster

401 kinetics in lithiation-delithiation.

402 Thus, engineering voids at the nanoscale, by direct introduction of specific porosity

403 during growth and producing alternated Si and C multi-layered nanocomposite films,

404 opens up the route for the effective use of silicon as lithium battery anode without the

405 need for any binder or conductive additive that would lower the overall energy density of

406 the resulting device. Further developments of this work shall include a thorough study of

407 the effects of annealing at lower temperatures, in view of larger scale applicability. This

408 would lead to a definition of an optimum temperature, i.e. the minimum one for the

409 stabilizing effect to occur, and provide useful information for the successive integration

410 of the annealing step into the deposition process, by means of a heated sample-holder.

411 This would further reduce fabrication steps, making it possible to deposit and anneal

412 silicon and carbon in one single processing step.

413 **Acknowledgements**

417

References

419 1.   Whittingham, M. S. Materials Challenges Facing Electrical Energy Storage. *MRS*
420   *Bull.* **33,** 411–419 (2011).

421 2.   Si, Q. *et al.* A high performance silicon/carbon composite anode with carbon
422   nanofiber for lithium-ion batteries. *J. Power Sources* **195,** 1720–1725 (2010).

423 3.   Fister, T. T. *et al.* Lithium Intercalation Behavior in Multilayer Silicon Electrodes.
424   *Adv. Energy Mater.* **4,** 1301494 (2014).

425 4.   Li, W. *et al.* Germanium nanoparticles encapsulated in flexible carbon nanofibers
426   as self-supported electrodes for high performance lithium-ion batteries. *Nanoscale*
427   **6,** 4532–7 (2014).

428 5.   Goriparti, S. *et al.* Review on recent progress of nanostructured anode materials
429   for Li-ion batteries. *J. Power Sources* **257,** 421–443 (2014).

430 6.   Liu, Y., Ma, R., He, Y., Gao, M. & Pan, H. Synthesis, Structure Transformation,
431   and Electrochemical Properties of Li 2 MgSi as a Novel Anode for Li-lon
432   Batteries. *Adv. Funct. Mater.* **24,** 3944–3952 (2014).

433 7.   Obrovac, M. N. & Krause, L. J. Reversible Cycling of Crystalline Silicon Powder.
434   *J. Electrochem. Soc.* **154,** A103 (2007).

435 8.   Liu, X. H. *et al.* Size-dependent fracture of silicon nanoparticles during lithiation.
436   *ACS Nano* **6,** 1522–31 (2012).

437 9.   Kalnaus, S., Rhodes, K. & Daniel, C. A study of lithium ion intercalation induced
438   fracture of silicon particles used as anode material in Li-ion battery. *J. Power*
439   *Sources* **196,** 8116–8124 (2011).

440 10. Szczech, J. R. & Jin, S. Nanostructured silicon for high capacity lithium battery
441   anodes. *Energy Environ. Sci.* **4,** 56 (2011).

442 11. Gowda, S. R. *et al.* Three-dimensionally engineered porous silicon electrodes for
443   li ion batteries. *Nano Lett.* **12,** 6060–5 (2012).

444 12. Wu, H. *et al.* Engineering empty space between Si nanoparticles for lithium-ion
445   battery anodes. *Nano Lett.* **12,** 904–9 (2012).

446 13. Zhao, Y., Liu, X., Li, H., Zhai, T. & Zhou, H. Hierarchical micro/nano porous
447   silicon Li-ion battery anodes. *Chem. Commun. (Camb).* **48,** 5079–81 (2012).

448   14.   De Boor, J. *et al.* Temperature and structure size dependence of the thermal
449   conductivity of porous silicon. *EPL (Europhysics Lett.* **96,** 16001 (2011).

450   15.   Zhu, J., Gladden, C., Liu, N., Cui, Y. & Zhang, X. Nanoporous silicon networks as
451   anodes for lithium ion batteries. *Phys. Chem. Chem. Phys.* **15,** 440–3 (2013).

452   16.   Martineau, F. *et al.* Electrodeposition at room temperature of amorphous silicon
453   and germanium nanowires in ionic liquid. *IOP Conf. Ser. Mater. Sci. Eng.* **6,**
454   012012 (2009).

455   17.   Epur, R., Ramanathan, M., Beck, F. R., Manivannan, A. & Kumta, P. N.
456   Electrodeposition of amorphous silicon anode for lithium ion batteries. *Mater. Sci.*
457   *Eng. B* **177,** 1157–1162 (2012).

458   18.   Gu, J., Fahrenkrug, E. & Maldonado, S. Direct electrodeposition of crystalline
459   silicon at low temperatures. *J. Am. Chem. Soc.* **135,** 1684–7 (2013).

460   19.   Biserni, E. *et al.* Silicon algae with carbon Topping as thin-film anodes for
461   lithium-ion microbatteries by a two-step facile method. *J. Power Sources* **274,**
462   252–259 (2014).

463   20.   Biserni, E. *et al.* Room temperature fabrication of silicon nanocrystals by pulsed
464   laser deposition. *J. Nanoparticle Res.* **16,** 2461 (2014).

465   21.   Brunauer, S., Emmett, P. H. & Teller, E. Adsorption of Gases in Multimolecular
466   Layers. *J. Am. Chem. Soc.* **60,** 309–319 (1938).

467   22.   Sing, K. S. W. Reporting physisorption data for gas/solid systems with special
468   reference to the determination of surface area and porosity (Recommendations
469   1984). *Pure Appl. Chem.* **57,** 603–619 (1985).

470   23.   Passoni, L. *et al.* Hyperbranched quasi-1D nanostructures for solid-state dye-
471   sensitized solar cells. *ACS Nano* **7,** 10023–31 (2013).

472   24.   Casari, C. S. & Li Bassi, A. in *Advances in Laser and Optics Research* (ed. Arkin,
473   W. T.) **7,** 65–100 (Nova Science Publishers, Inc., 2012).

474   25.   Li, Z. *et al.* Raman characterization of the structural evolution in amorphous and
475   partially nanocrystalline hydrogenated silicon thin films prepared by PECVD. *J.*
476   *Raman Spectrosc.* **42,** 415–421 (2011).

477   26.   Richter, H., Wang, Z. P. & Ley, L. The one phonon Raman spectrum in
478   microcrystalline silicon. *Solid State Commun.* **39,** 625–629 (1981).

479   27.   Duan, Y., Kong, J. F. & Shen, W. Z. Raman investigation of silicon nanocrystals:
480   quantum confinement and laser-induced thermal effects. *J. Raman Spectrosc.* **43,**
481   756–760 (2012).

482   28.   Bruno, P. *et al.* Pulsed Laser Deposition of Silicon Nanostructures. *MRS Proc.*
483   **1322,** mrss11–1322–b05–34 (2011).

484   29.   Kasavajjula, U., Wang, C. & Appleby, A. J. Nano- and bulk-silicon-based
485   insertion anodes for lithium-ion secondary cells. *J. Power Sources* **163,** 1003–
486   1039 (2007).

487   30.   Li, X. *et al.* Mesoporous silicon sponge as an anti-pulverization structure for high-
488   performance lithium-ion battery anodes. *Nat. Commun.* **5,** 1–7 (2014).

489   31.   Green, M., Fielder, E., Scrosati, B., Wachtler, M. & Moreno, J. S. Structured
490   Silicon Anodes for Lithium Battery Applications. *Electrochem. Solid-State Lett.* **6,**
491   A75 (2003).

492   32.   Kawamura, T., Okada, S. & Yamaki, J. Decomposition reaction of LiPF6-based
493   electrolytes for lithium ion cells. *J. Power Sources* **156,** 547–554 (2006).

494   33.   Lux, S. F. *et al.* The mechanism of HF formation in LiPF6 based organic
495   carbonate electrolytes. *Electrochem. commun.* **14,** 47–50 (2012).

496   34.   Aurbach, D. *et al.* Recent studies on the correlation between surface chemistry,
497   morphology, three-dimensional structures and performance of Li and Li-C
498   intercalation anodes in several important electrolyte systems. *J. Power Sources* **68,**
499   91–98 (1997).

500   35.   Heider, U., Oesten, R. & Jungnitz, M. Challenge in manufacturing electrolyte
501   solutions for lithium and lithium ion batteries quality control and minimizing
502   contamination level. *J. Power Sources* **81-82,** 119–122 (1999).

503   36.   Ferrari, A. C. & Robertson, J. Interpretation of Raman spectra of disordered and
504   amorphous carbon. *Phys. Rev. B* **61,** 14095–14107 (2000).

505   37.   Ferrari, A. C. & Robertson, J. Raman spectroscopy of amorphous, nanostructured,
506   diamond−like carbon, and nanodiamond. *Philos. Trans. R. Soc. A* **362,** 2477–2512
507   (2004).

508   38.   Hassan, F. M., Chabot, V., Elsayed, A. R., Xiao, X. & Chen, Z. Engineered si
509   electrode nanoarchitecture: a scalable postfabrication treatment for the production
510   of next-generation li-ion batteries. *Nano Lett.* **14,** 277–83 (2014).

511